Relationship between electrical properties and crystallization of indium oxide thin films using ex-situ grazing-incidence wide-angle x-ray scattering

G. B. González, J. S. Okasinski, D. B. Buchholz, J. Boesso, J. D. Almer, L. Zeng, M. J. Bedzyk, and R. P. H. Chang

Citation: Journal of Applied Physics **121**, 205306 (2017); doi: 10.1063/1.4984054
View online: https://doi.org/10.1063/1.4984054
View Table of Contents: http://aip.scitation.org/toc/jap/121/20
Published by the American Institute of Physics

Relationship between electrical properties and crystallization of indium oxide thin films using *ex-situ* grazing-incidence wide-angle x-ray scattering

G. B. González,[1] J. S. Okasinski,[2] D. B. Buchholz,[3] J. Boesso,[1] J. D. Almer,[2] L. Zeng,[4] M. J. Bedzyk,[3,4] and R. P. H. Chang[3]
[1]*Department of Physics, DePaul University, Chicago, Illinois 60614, USA*
[2]*Advanced Photon Source, Argonne National Laboratory, Argonne, Illinois 60439, USA*
[3]*Department of Materials Science and Engineering, Northwestern University, Evanston, Illinois 60208, USA*
[4]*Graduate Program in Applied Physics, Northwestern University, Evanston, Illinois 60208, USA*

(Received 17 January 2017; accepted 10 May 2017; published online 25 May 2017)

Grazing-incidence, wide-angle x-ray scattering measurements were conducted on indium oxide thin films grown on silica substrates via pulsed laser deposition. Growth temperatures (T_G) in this study ranged from −50 °C to 600 °C, in order to investigate the thermal effects on the film structure and its spatial homogeneity, as well as their relationship to electrical properties. Films grown below room temperature were amorphous, while films prepared at $T_G = 25$ °C and above crystallized in the cubic bixbyite structure, and their crystalline fraction increased with deposition temperature. The electrical conductivity (σ) and electrical mobility (μ) were strongly enhanced at low deposition temperatures. For $T_G = 25$ °C and 50 °C, a strong ⟨100⟩ preferred orientation (texture) occurred, but it decreased as the deposition temperature, and consequential crystallinity, increased. Higher variations in texture coefficients and in lattice parameters were measured at the film surface compared to the interior of the film, indicating strong microstructural gradients. At low crystallinity, the in-plane lattice spacing expanded, while the out-of-plane spacing contracted, and those values merged at $T_G = 400$ °C, where high μ was measured. This directional difference in lattice spacing, or deviatoric strain, was linear as a function of both deposition temperature and the degree of crystallinity. The crystalline sample with $T_G = 100$ °C had the lowest mobility, as well as film diffraction peaks which split into doublets. The deviatoric strains from these doublet peaks differ by a factor of four, supporting the presence of both a microstructure and strain gradient in this film. More isotropic films exhibit larger μ values, indicating that the microstructure directly correlates with electrical properties. These results provide valuable insights that can help to improve the desirable properties of indium oxide, as well as other transparent conducting oxides. *Published by AIP Publishing.* [http://dx.doi.org/10.1063/1.4984054]

I. INTRODUCTION

Transparent conducting oxides (TCOs) are used in a wide variety of applications due to their high transparency in the visible region and high electrical conductivity.[1] The unique combination of electrical and optical properties of these materials is exploited in commercial applications including photovoltaics and optoelectronic devices.[2–4] Recently, in several technological applications, such as flat-panel displays, an increased number of amorphous oxide semiconducting (AOS) films are being utilized.[5] AOSs are deposited at lower temperatures,[6] and sometimes they can exhibit smoother surfaces[7,8] and better mechanical properties[9,10] while still maintaining the optical and electrical properties of crystalline TCOs.[11] Synthesis conditions of TCOs affect the structure, microstructure, and useful properties of the films. The choice of deposition temperature and degree of crystallinity is based on what properties need to be optimized for a specific application. Amorphous and partially crystalline TCO films have been investigated for flexible organic light-emitting diode applications where the electrodes are deposited on polymer substrates. While the amorphous films had the highest electrical conductivities, the optical and mechanical properties of the partially crystalline films were better.[12] Recent experiments also showed that the thermoelectric conductivity of partially crystalline TCO films is higher compared to amorphous or crystalline films.[13]

Commonly used TCOs and AOSs consist of oxides of indium, tin, gallium, cadmium, and zinc. Indium-tin oxide (ITO) is obtained by doping indium oxide (IO) with tin. ITO has better electrical properties than undoped indium oxide and is the material of choice for flat-panel displays. The structure of crystalline IO[14] and the defect structure of crystalline ITO[15] have been determined from diffraction experiments. The bixbyite structure of In_2O_3 is cubic with a lattice parameter of 10.117 Å and space group $Ia\bar{3}$.[14] One unit cell contains 32 indium cations and 48 oxygen anions. Doping IO with tin increases the lattice parameter as tin substitutes into the indium sites, and additional oxygen occupies interstitial sites; however, the cubic bixbyite structure is maintained.[15]

The deposition temperature, deposition rate, and gas pressure affect the crystallinity of TCO films. For a fixed oxygen partial pressure (pO_2), lower deposition temperatures result in less crystalline films.[16–18] A similar effect is seen while lowering pO_2 if T_G is constant in ITO films.[19,20] The effects of argon and oxygen partial pressure on crystallinity and on the electrical and optical properties of indium-zinc oxide (IZO) grown via pulsed laser deposition (PLD) have also been investigated.[21] The highest mobility (μ) was measured on amorphous samples, but the highest electron concentrations were

obtained for crystalline IZO films. Another study on the effect of oxygen partial pressure revealed that as pO_2 increased from 0.13 Pa to 2.7 Pa, the crystallinity of ITO films increased.[20] The splitting of diffraction peaks in ITO semi-crystalline films prepared by magnetron sputtering,[22] e-beam evaporation,[22] and pulsed-laser deposition[19–21,23] has been observed, and this effect was attributed to the presence of two differently strained layers in films more than 200 nm thick.

Studies of amorphous undoped IO films deposited by PLD indicate an effect of deposition temperature on the structure and electrical properties.[18] The carrier mobility decreased with decreasing deposition temperature, as did the density of the amorphous films. A local maximum in μ was observed at a deposition temperature just below the temperature at which crystallinity can first be observed by diffraction and where the density was the same as in a fully crystalline film.[16] The mobility decreased both at lower and higher deposition temperatures, but once highly crystalline films were obtained, μ again increased.[17] EXAFS and molecular dynamics simulations related the local mobility maxima to structural factors. The amorphous and highly crystalline structures of zinc-indium-tin oxide (ZITO) have also been reported,[18,24,25] and a local maximum in μ just prior to the observation of crystallization is also observed.[18]

The interplay between the structure and properties revealed by amorphous and crystalline films warrants a closer look, with the promise of yielding insights that could be used to further improve and expand the applications of these films. As mentioned earlier, partially crystalline ITO films can sometimes have better mechanical, optical, and thermoelectric properties than fully amorphous films, even when their electrical conductivity is lower.[12] The thermal conductivity of semi-crystalline indium-gallium zinc oxide (IGZO) films can also be higher than that of amorphous or fully crystalline samples.[13] A better understanding of the depth and lateral uniformity of the crystalline films is also crucial in understanding specific properties. For example, in materials such as graphene oxide, the in-plane and cross-plane thermal conductivities can vary by a factor of 675.[26] Such high anisotropic thermal conductivity is exploited for thermal management in electronic applications, wherein thermal pads effectively remove heat in the large in-plane area and protect components underneath from heating.[26] In Ge/Si films, electronic transport has also been found to be anisotropic since the cross-plane electrical conductivity was measured to be five times lower than in-plane.[27] While these types of experiments have not been reported in TCOs, it is expected that the microstructural anisotropy of the films plays a major role in these anisotropic properties.

In the present study, a series of nine thin films of In_2O_3 were prepared at different deposition temperatures keeping pO_2 constant. The purpose of studying IO is to focus on the parent undoped bixbyite structure and eliminate the effect of dopants which add complexity to the defect structure. The electrical conductivity, mobility, and carrier concentration of the samples were measured. The degree of crystallinity, lattice parameters, deviatoric strain, peak broadening, and texture of the films were determined by analyzing x-ray diffraction data using grazing incidence geometry. Diffraction data were collected at two different incident angles to study the depth uniformity of the films. The lateral homogeneity of the films was studied by collecting data along the in-plane (IP) and out-of-plane (OP) directions. These investigations provide an increased understanding of structural and microstructural changes during the crystallization process and their effect on properties. This knowledge can help to improve the desirable properties of indium-based bixbyite oxides such as ITO, as well as other TCOs.

II. EXPERIMENTAL PROCEDURE

Nine indium oxide films were prepared using PLD on amorphous silica substrates at different growth temperatures: $T_G = -50\,^{\circ}C$, $0\,^{\circ}C$, $25\,^{\circ}C$, $50\,^{\circ}C$, $75\,^{\circ}C$, $100\,^{\circ}C$, $200\,^{\circ}C$, $400\,^{\circ}C$, and $600\,^{\circ}C$. The films were grown from a dense hot-pressed indium oxide target (25 mm diameter). PLD was accomplished with a 248 nm KrF excimer laser with a pulse duration of 25 ns and operated at 2 Hz. The 200 mJ/pulse beam was focused onto a 1 mm × 2 mm spot size. The target was rotated at 5-rpm about its axis to prevent localized heating. The target-substrate separation was fixed at 10 cm. The films were grown on fused-silica substrates in an O_2 ambient of 8 mTorr. The substrates were attached to the substrate holder with silver paint. For films grown above room temperature, a resistively heated substrate-holder was used; for films grown below room temperature, the substrate was cooled using liquid nitrogen. Deposition times were on the order of 2 h. The power to the heaters was turned off, and natural cooling (or heating) occurred, lasting 2–3 h, to bring the films to room temperature. The samples were approximately 1 cm × 1 cm.

The sheet resistance (R_s: Ω/□), carrier type, area carrier-concentration (n_a: 1/cm^2), and carrier mobility (μ_H: cm^2/V s) were measured with an Ecopia 3000 Hall measurement system on samples in the van der Pauw geometry. The carrier density (n_v: 1/cm^3) and resistivity (ρ: Ω cm) were calculated by dividing the area carrier-concentration and sheet resistance, respectively, by the film thickness. The film thickness was measured using a spectral reflectometer (Filmetrics F20). The average thickness of the films was 375 nm.

Grazing-incidence, wide-angle x-ray scattering (GIWAXS) data were measured at room temperature using 70 keV x-rays and a unique multi-panel detector array at the 1-ID beamline of the Advanced Photon Source at the Argonne National Laboratory. A schematic of the experimental geometry is shown in Fig. 1. The use of a grazing-incidence geometry is beneficial when studying thin films because the x-ray penetration depth can be tuned to be on the order of the film thickness with a correspondingly high film/substrate scattering ratio. The incident beam size was 37 μm × 100 μm wide using vertical focusing and horizontal slits. Diffraction data up to $Q = 8.7\,\text{Å}^{-1}$ were collected using four General Electric (GE) detectors at a nominal distance from the sample of 1746 mm. Each detector had 2048 × 2048 pixels, with a pixel size of 200 μm × 200 μm. To explore any changes in the local structure as a function of distance from the surface, data were measured from two penetration depths: near the critical angle ($\omega = 1\alpha_c$) and at twice the critical

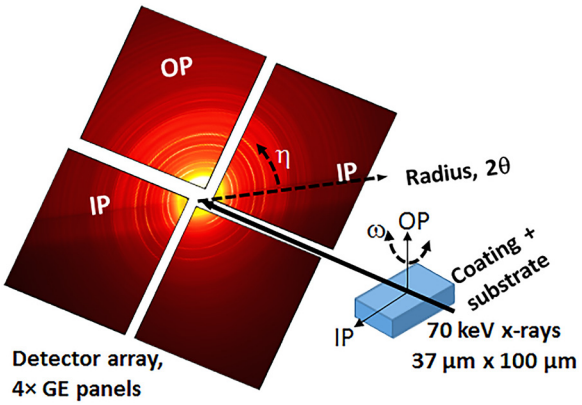

FIG. 1. Geometry and four-panel detector array used to collect data. The left and right detectors probe the in-plane (IP) or horizontal direction, while the top detector measures the out-of-plane (OP) or vertical direction. The azimuthal angle is η, and ω is the tilt angle relative to the surface normal. The diffraction data shown in this figure correspond to the indium oxide sample deposited at 400 °C for $\omega = 2\alpha_c$.

angle ($\omega = 2\alpha_c$). The critical angle was experimentally determined for all films by rocking the sample and observing the position of the reflected beam on an area detector. These angles were found to be consistent with the critical angle of 0.042°, calculated using the procedure described in Ref. 28, and an electron density of 1.0 e/Å^3 (Ref. 16) for In_2O_3. At this critical angle, the penetration depth is 24 nm. The data collected with the incident angle set at $\omega = 1\alpha_c$ enhanced the near-surface signal from the films. The entire film thickness of the samples was measured by setting the incident angle to $\omega = 2\alpha_c$ since the calculated penetration depth was 510 nm, which is larger than the thickness of the films. By measuring at these two angles, the presence of possible thickness gradients in the films was assessed.

The sample geometry (sample-detector distance, detector tilts, and beam center) was calibrated using powder standards 660a (LaB_6) and 674b (CeO_2) obtained from NIST. The calibrations were performed with Fit2d,[29] and subsequent 2D radial integrations over select orientations were performed using custom MATLAB scripts.[30] The data for each detector were integrated over an azimuthal range of $\eta = 20°$, centered about the principal orientations (surface normal and in-plane) in the sample. As shown in Fig. 1, the left and right detectors collected the in-plane directions, while the top and bottom detectors measured the out-of-plane orientation. The IP values reported were obtained from averaging the left and right detector results. The data obtained from the bottom detector were not analyzed due to absorption effects.

Ten individual reflections were fitted using pseudo-Voigt functions in order to obtain the positions and widths of the peaks, as well as their integrated intensities for the crystalline samples deposited at $T_G = 50$ °C, 75 °C, 100 °C, 200 °C, 400 °C, and 600 °C. The deviatoric strain was calculated using the fitted d-spacing for each reflection along the in-plane and out-of-plane directions, as shown in the following equation:

$$\text{Deviatoric strain} = \frac{d_{\text{in plane}} - d_{\text{out of plane}}}{d_{\text{in plane}}}. \quad (1)$$

The texture coefficient (TC_{hkl}) along each reflection was calculated using the integrated intensities and the following equation:

$$TC_{hkl} = \left| \frac{I_{\text{in plane}} - I_{\text{out of plane}}}{I_{\text{max (of in plane or out of plane)}}} \right|_{hkl}. \quad (2)$$

From the GI-WAXS diffraction patterns, the In_2O_3 thin films with sequenced deposition temperatures have presented an amorphous-to-crystalline transition. Therefore, the quantification of the film crystallinity has also been conducted to illustrate the effects induced by initial PLD conditions. The data were calibrated and integrated using GSAS II[31] over an azimuthal range of 140° using the left, top, and right detectors shown in Fig. 1. The degree of crystallinity χ_c is usually defined as the ratio of the areas under the crystalline peaks over that of under the whole background-subtracted XRD patterns. However, in our case, some of the films are textured and anisotropic, and so, the line profiles either along the IP or OP direction alone would not be sufficient to determine the degree of crystallinity. Therefore, it is necessary to divide the diffraction rings of GI-WAXS patterns into individual segments and calculate them separately. The reflected diffraction rings in the upper half of the 2-D GI-WAXS patterns were divided into three segments. Three individual 1-D diffraction patterns were extracted and integrated for each segment, and the degree of crystallinity χ_c was calculated as indicated by the following equation:

$$\chi_c = \frac{\sum_{i=1}^{3} \int_{Q_0}^{Q_f} I_c(Q)\,dQ}{\sum_{i=1}^{3} \int_{Q_0}^{Q_f} I(Q)\,dQ}, \quad (3)$$

where $I_c(Q)$ is the crystalline peak intensity and $I(Q)$ is the intensity of the coherent x-rays scattered from the sample films (after the subtraction of background and SiO_2 substrate peaks). A pseudo-Voigt function was used to fit each (amorphous or crystalline) peak. The uncertainty for χ_c was obtained by propagating the error in each peak integrated intensity. The data analysis focused on GI-WAXS data taken at $2\alpha_c$ incident conditions for films with $T_G = 25$–400 °C.

III. RESULTS AND DISCUSSION

Figure 2 shows the integrated intensity for the samples along the IP and OP directions for both depths, as well as the XRD pattern calculated for cubic bixbyite In_2O_3. The data at the critical angle ($1\alpha_c$) probe the surface of the film, while the data collected at two times the critical angle ($2\alpha_c$) penetrate through the entire film thickness. The XRD patterns for the samples deposited below room temperature only exhibit broad peaks, indicating that the films are amorphous. Above room temperature, sharp features in the XRD patterns appear due to crystallization. These diffraction peak positions correspond to the cubic bixbyite structure for indium oxide. For $T_G = 25$ °C and 50 °C, along the IP direction, the (400)

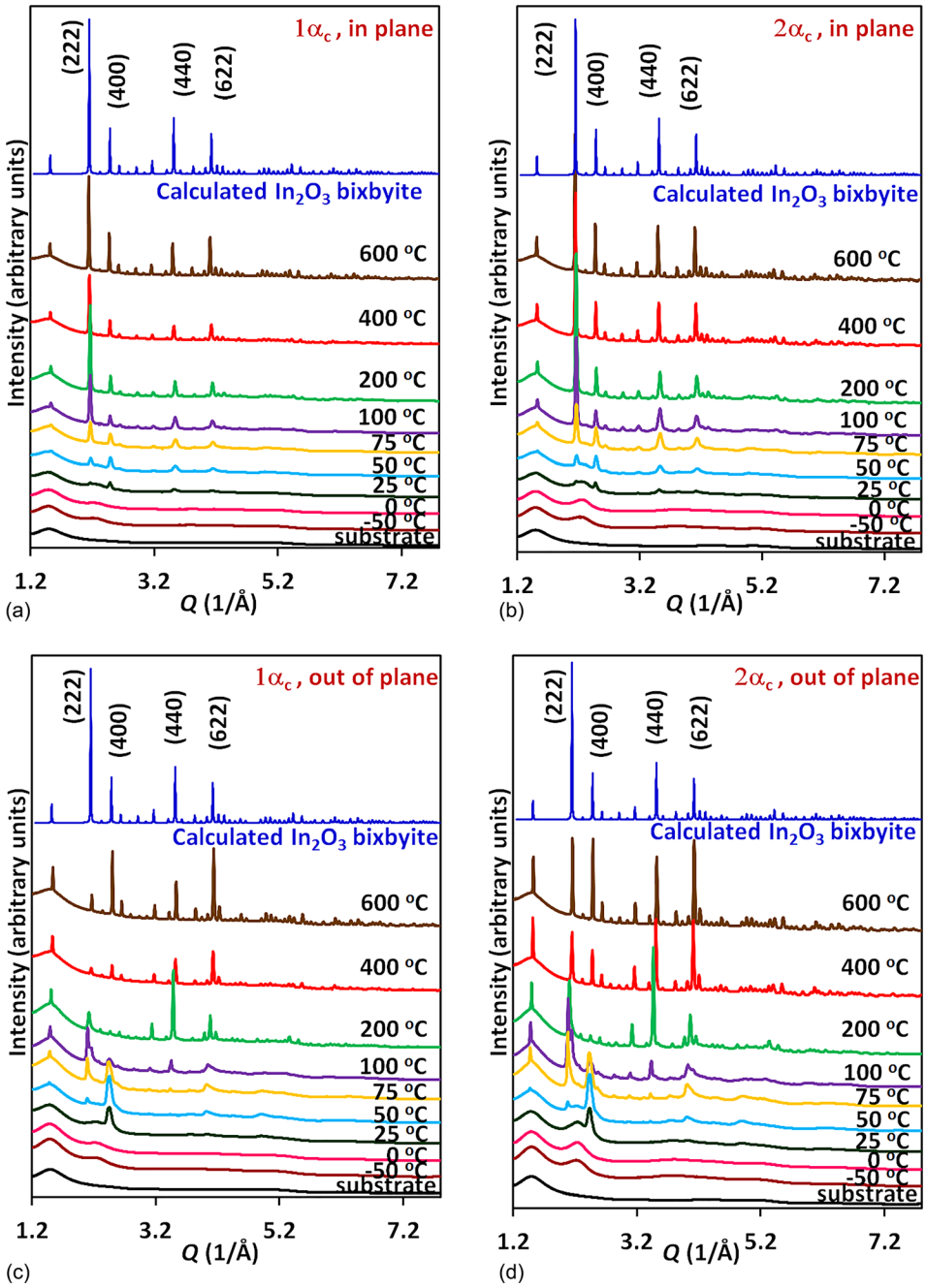

FIG. 2. X-ray diffraction patterns as a function of deposition temperature: (a) in-plane direction at $1\alpha_c$, (b) in-plane direction at $2\alpha_c$, (c) out-of-plane direction at $1\alpha_c$, and (d) out-of-plane direction at $2\alpha_c$. The X-ray diffraction pattern for the In_2O_3 cubic bixbyite structure calculated at 70 keV is also shown for comparison purposes.

diffraction peak has the highest intensity, indicating that the first grains at low temperatures orient along this crystallographic direction. These peaks are even more intense along the OP direction, especially for the $2\alpha_c$ incident angle, showing that in these films, the crystal structure is well-aligned to the surface normal. As the deposition temperature increases, other bixbyite diffraction peaks appear, and the (400) preferred orientation diminishes.

Along the OP direction, the relative intensities of the XRD patterns deviate the most from the calculated powder pattern of polycrystalline IO. The relative intensities along the IP direction match closer the pattern of bixbyite IO, especially at the highest deposition temperatures. Differences in the data collected at different incident angles show that the films have depth gradients as well. The film interior ($2\alpha_c$) patterns resemble more the ideal IO structure, indicating that the last material that deposits at the top of the film (probed by the $1\alpha_c$ measurements) is more distorted compared to the bottom region of the sample. Furthermore, as seen in Fig. 3, there are shifts in the peak positions between the $1\alpha_c$ and $2\alpha_c$ data, demonstrating that there is some strain gradient in the partially crystalline films. Smaller lattice parameters are measured at the surface compared to the bulk of the film, and the shifts are more pronounced along the out-of-plane direction.

For $T_G = 75\,^{\circ}\mathrm{C}$ and $100\,^{\circ}\mathrm{C}$, the diffraction peaks are asymmetric, and there is splitting of the reflections in the out-of-plane direction. At higher growth temperatures, the diffraction peaks become more symmetric and the splitting disappears, as shown in Fig. 3(a). The largest splitting of the (222) reflection occurs for $T_G = 100\,^{\circ}\mathrm{C}$. The stronger peak located at lower angles is labeled Peak 1. The ratios of Peak 1/Peak 2 for $1\alpha_c$ *vs* $2\alpha_c$ are the following: 2.4 *vs* 1.8 for

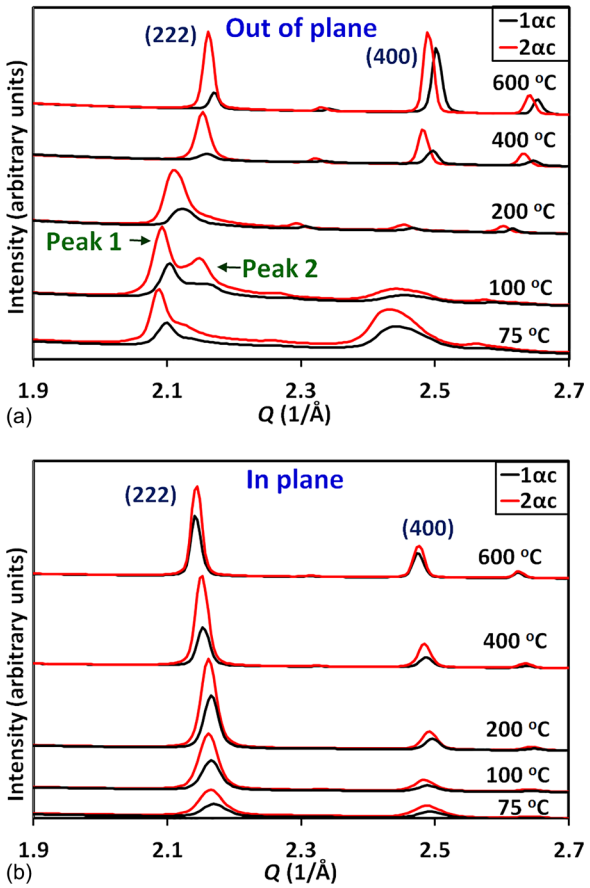

FIG. 3. XRD patterns measured at $1\alpha_c$ and $2\alpha_c$ for $T_G = 75\,^{\circ}\text{C}$, $100\,^{\circ}\text{C}$, $200\,^{\circ}\text{C}$, $400\,^{\circ}\text{C}$, and $600\,^{\circ}\text{C}$. (a) The splitting of the (222) peak is enhanced for $T_G = 100\,^{\circ}\text{C}$ in the out-of-plane direction. (b) splitting and asymmetry are absent in the in-plane direction.

maximum peak intensities, 1.4 *vs* 1.1 for integrated intensities, 0.5 *vs* 0.6 for FWHM, and 1.024 *vs* 1.026 for *d*-spacings. This analysis shows that Peak 1 is enhanced at the surface of the film compared to the bulk. This splitting is not observed along the in-plane direction, as seen in Fig. 3(b). For Peak 1, the deviatoric strain, calculated using Eq. (1), is -0.03 for both depth measurements, which is larger by a factor of more than four for Peak 2 (deviatoric strain is -0.007 for $2\alpha_c$ and -0.006 for $1\alpha_c$). Studies on ITO films deposited by DC magnetron sputtering reported similar splitting of diffraction peaks and attributed this effect to the existence of two differently strained layers in the films.[22] According to this model, a weakly strained layer crystallizes from the as-deposited amorphous material near the substrate due to thermal annealing during deposition, while the strongly strained layer at the top is an as-deposited crystalline layer.[22] The present IO data are consistent with this model: Peak 1 is associated with the strongly strained, as-deposited top layer, while Peak 2 corresponds to the weakly strained bottom layer that crystallizes from the amorphous material deposited near the substrate. ITO films grown by PLD also report peak splitting for partially crystalline samples[19,20,23] that are ~400 nm thick, but the splitting does not occur for films less than 200 nm thick.[20] Izumi *et al.* reported that in ITO films grown at a fixed T_G of 200 °C, the largest peak splitting in the out-of-plane direction occurred at $pO_2 = 0.67$ Pa; at lower pO_2, the peaks of the less crystalline film were asymmetric, but at higher pO_2 (1.3 Pa and 2.7 Pa), crystallinity increased while the peaks became more symmetric.[20] Figure 3(a) shows a similar relationship between the peak shape and crystallinity for undoped IO with comparable thicknesses, except that as seen in Fig. 4, in the present study, the crystallinity changes with T_G, while pO_2 is constant. Increasing pO_2 at a fixed T_G in ITO films has the same effect as increasing T_G at a fixed pO_2 in IO: semi-crystalline films have asymmetric or even split peaks that evolve into higher peak symmetry for more crystalline samples. These interesting structural and microstructural changes correlate well with measured electrical properties, as will be discussed later.

The behavior of the lattice parameter (a) is presented in Fig. 5. As the samples become more crystalline, a increases slightly in the in-plane direction but decreases more significantly (approximately three times more) in the out-of-plane direction. For $T_G = 400\,^{\circ}\text{C}$, a values of both directions merge, and in the bulk, they intersect the horizontal red line that represents the unit cell size of cubic bixbyite ($a = 10.117$ Å). At the surface, this high lateral isotropy occurs slightly below the red line, indicating that there is still some depth gradient in that sample.

The deviatoric strain, calculated using Eq. (1) and shown in Fig. 6, is linear with deposition temperature and ranges from -4.0% to 1.5%. For the samples exhibiting asymmetric or split diffraction peaks, the positions of Peak 1 were used in these calculations. The deviatoric strain is compressive for T_G below 200 °C and tensile for $T_G = 400\,^{\circ}\text{C}$ and 600 °C. The data in Fig. 6 generally fall under the expected bounding values of $\langle 111 \rangle$ and $\langle 100 \rangle$ directions. The differences indicate that the $\langle 111 \rangle$ direction is the softest, while the $\langle 100 \rangle$ direction is the stiffest. These results show that there is elastic anisotropy through the multiple *hkl* measured. To the authors' knowledge, no elastic constant measurements have been reported in the literature for undoped indium oxide. Guo *et al.* determined the elastic constants using coherent acoustic vibrations of uniform tin-doped indium oxide nano-rod arrays.[32] The calculated Young's moduli of these ITO nano-rods were $E_{[100]} = 217.9$ GPa, $E_{[110]} = 110.5$ GPa, and $E_{[111]} = 94.9$ GPa. These ITO values

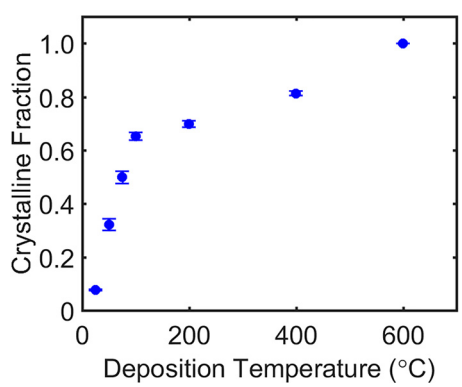

FIG. 4. Fraction of crystallinity in the samples as a function of deposition temperature, obtained using Eq. (3). A pseudo-Voigt function was used to fit each (amorphous or crystalline) peak. The uncertainties were obtained by propagating the error in each peak integrated intensity.

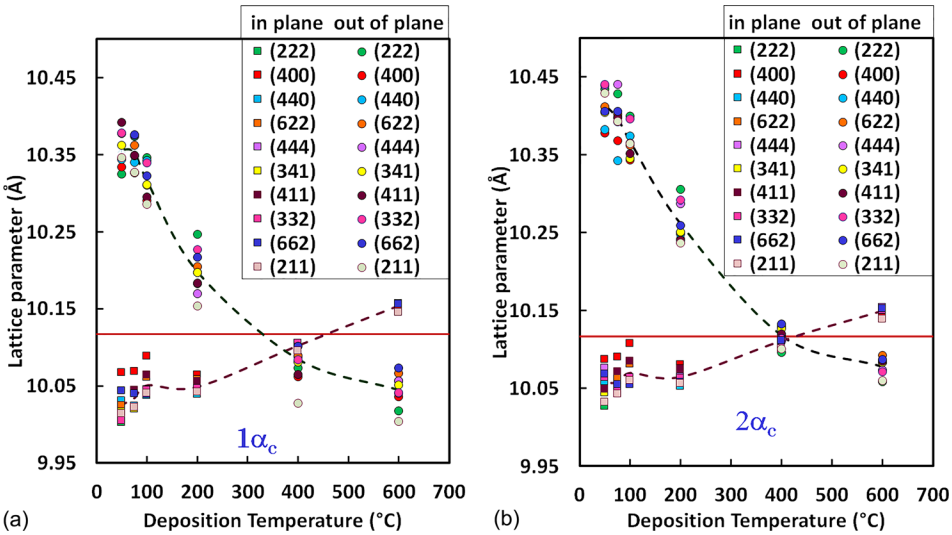

FIG. 5. Lattice parameters as a function of growth temperature: (a) surface and (b) film bulk. The horizontal red line corresponds to 10.117 Å, the lattice parameter of polycrystalline cubic bixbyite IO. The dashed lines correspond to the out-of-plane and in-plane averages of all *hkl* reflections. Uncertainties from the fits were on the order of $(a \times 2 \times 10^{-4})$ Å, which are smaller than the symbol size.

agree with the *hkl*-dependent trends observed for IO in the present study.

The largest deviation in the lattice parameter occurs for the least crystalline samples in the out-of-plane direction, consistent with higher lattice distortion. For the most crystalline samples, the film interior lattice parameters, obtained using a higher incident angle, are closer to the unit cell size of bixbyite indium oxide. Several factors might contribute to the observed behavior of strain in these films. For the most crystalline film, deposited at $T_G = 600\,^{\circ}\mathrm{C}$, differences in coefficients of thermal expansion (CTE) between the film values and the substrate could be the major cause of strain when samples are quenched to room temperature. Values for CTE of ITO between $7.2 \times 10^{-6}\,^{\circ}\mathrm{C}^{-1}$ and $10.2 \times 10^{-6}\,^{\circ}\mathrm{C}^{-1}$ have been reported in the literature.[33,34] The amorphous silica substrate has a CTE of $0.55 \times 10^{-6}\,^{\circ}\mathrm{C}^{-1}$;[35] therefore, upon cooling, the crystalline IO will contract more than the substrate. The effect of deposition at an elevated temperature and cooling should result in an in-plane tensile stress on the film that would yield a larger lattice parameter. For the fully crystalline film deposited at 600 °C and cooled to room temperature, there would be a difference of ~0.5% (0.05 Å), which is actually seen for the film bulk in-plane lattice constant. The contraction of the out-of-plane lattice parameter could be attributed to the Poisson effect.

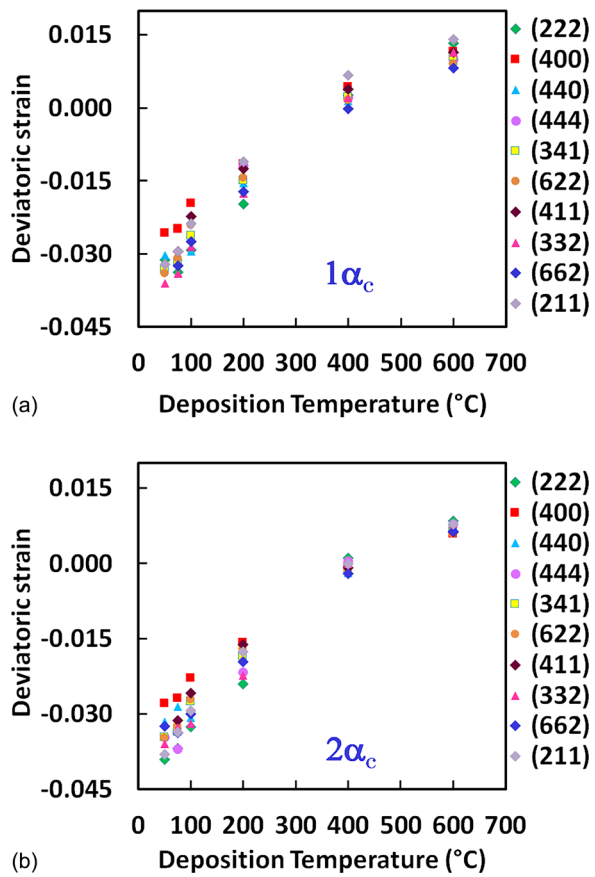

FIG. 6. Deviatoric strain, calculated using Eq. (1), as a function of deposition temperature measured at (a) $1\alpha_c$ and (b) $2\alpha_c$. Propagated uncertainties from the fits are smaller than the symbol size and were on the order of 0.0003.

Strain associated with CTE differences between the substrate and the film would be smaller at lower deposition temperatures since the difference between T_G and room temperature is smaller. Furthermore, at lower deposition temperatures, the films are a mixture of amorphous and crystalline materials. For the semi-crystalline films near $T_G = 100\,^{\circ}\mathrm{C}$, the model with two different strained layers was consistent with diffraction peak splitting. PLD provides directed energy to the species that impinge on the substrate causing strain. However, when the substrate is heated, lateral diffusion relieves some of the strain in the films. This is consistent with the low deviatoric strain measured for Peak 2 corresponding to the layer near the substrate. Peak 1, attributed mainly to the surface layer, exhibited higher deviatoric strain (4–5 times higher). This top layer is further away from the heated substrate and has less time to diffuse since it is the last material to be deposited. Using literature values (1×10^{-15} cm^2/s, at 200 °C) of oxygen diffusion in ITO films deposited from an ion sputtered In target in an oxygen gas background,[36] the diffusion time for 400 nm thick films would correspond to 10^6 s, which is two orders of magnitude longer than the deposition and quenching times of the IO films. However, one needs to take into account that the IO films from PLD were ablated from an IO target in an oxygen gas medium layer by layer at a very

slow rate of ~0.07 nm/s. This might greatly reduce the diffusion time. The deviatoric strain in the films decreased as T_G was further increased, consistent with slower diffusion at lower temperatures.

The film density and significant changes in stoichiometry are not expected to play a major role in the strain of crystalline IO films. In thinner PLD IO films (~60 nm thick), the density of amorphous films grown at −50 °C decreased by ~15% compared to films grown at +50 °C.[16] In that study, the first crystalline films occurred at $T_G = 75$ °C, which is 50 °C higher than in the present study with 400 nm films. For thicker films, there might be similar trends in density for amorphous films; however, it is expected that thicker IO films that show any crystallinity are as dense as the fully crystalline ones. XPS measurements on the thinner IO films showed that all the samples had the same In/O ratio within ±5%, and there was no observable trend as a function of deposition temperature.[16] Therefore, it is expected that the present films do not have significant changes in composition either.

The depth gradient in the partially crystalline films can be evaluated from Figs. 3, 5, and 6. Smaller lattice parameters are measured for the surface compared to the bulk of the film, and the shifts are more pronounced along the out-of-plane direction. The lattice parameter differences in the out-of-plane direction between the surface and film interior for $T_G = 75$ °C, 100 °C, 200 °C, 400 °C, and 600 °C are 0.141%, 0.149%, 0.106%, −0.029%, and −0.090%. The corresponding differences for the in-plane direction are −0.062%, −0.007%, −0.005%, −0.002%, and −0.004%, which are much smaller. The most crystalline samples have higher depth isotropy, which is not surprising, since at higher temperatures, the diffusion of atoms is enhanced, allowing them to arrange themselves in a more orderly manner throughout the film.

As previously mentioned, the IO crystals in the films deposited at the onset temperature showed a strong (400) preferred orientation, which was more pronounced in the out-of-plane direction. As crystallization progressed at higher temperatures, this preferred orientation decreased. Figure 1 shows the 2D diffraction images for $T_G = 400$ °C, where it is evident that texture was present since the intensities of the diffraction rings were not uniform. TC_{222} and TC_{332}, calculated using Eq. (2), increased with deposition temperature and plateaued at 400 °C at the film surface, as seen in Fig. 7(a). On the other hand, TC_{440} decreased with deposition temperature. In the film interior, the texture differences were less pronounced but followed similar trends as at the surface. TC_{hkl} values for the other reflections that were analyzed were, within experimental error, essentially random and showed no deposition temperature dependence.

Figure 8 shows the behavior of the peak broadening as a function of deposition temperature for the measurements performed at $2\alpha_c$, corresponding to the entire film thickness. As expected, the peaks became narrower at higher deposition temperatures, indicating that grain growth occurred. At low temperatures, the IP direction has broader peaks compared to the film growth direction. At the highest deposition temperatures, both FWHM values merge, indicating that the grains become more isotropic.

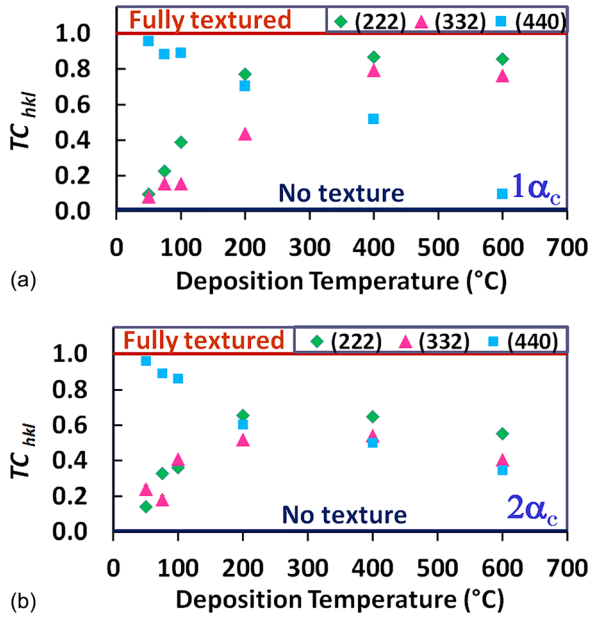

FIG. 7. Texture coefficient (TC_{hkl}), calculated using Eq. (2), as a function of deposition temperature at (a) $1\alpha_c$ and (b) $2\alpha_c$. $TC_{hkl} = 0$ corresponds to no texture, while $TC_{hkl} = 1$ corresponds to fully textured. Propagated uncertainties from the fitted integrated intensities are smaller than the symbol size and ranged from 0.001 to 0.002.

The carrier concentration, electrical mobility, and conductivity of these films are shown in Fig. 9. The Hall measurements represent average values of these electrical properties in the bulk of the film. The carrier concentration of films below $T_G = 100$ °C was nearly constant, and it decreased for the most crystalline samples. At low temperatures, the films are more amorphous and more defective. The interface between the crystallites and the amorphous phase could act as a source of ionized oxygen defects. In IO, ionized oxygen vacancies are charge-compensated with free electrons, resulting in a higher carrier concentration. However, at higher temperatures, as the samples are becoming more ordered and more crystalline, the defects decrease, lowering the carrier concentration.

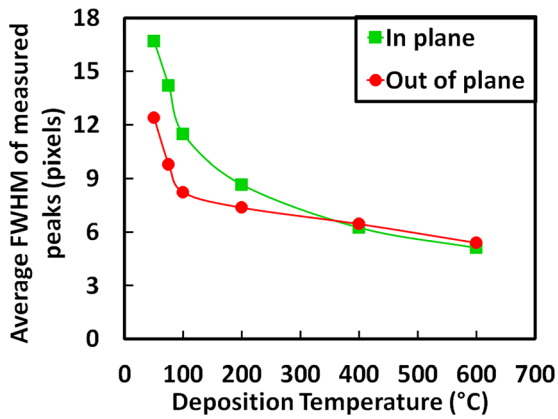

FIG. 8. Average full width at half maximum (FWHM) of the *hkl* reflections measured at $2\alpha_c$, as a function of growth temperature. Propagated uncertainties in the FWHM obtained from the fitted peaks were on the order of 2%, which are smaller than the symbol size.

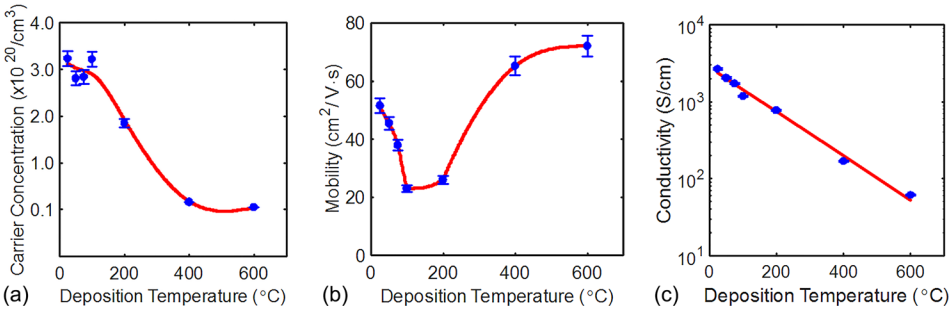

FIG. 9. (a) Carrier concentration, (b) electrical mobility, and (c) electrical conductivity, as a function of deposition temperature. The uncertainties correspond to the standard deviation of measurements on multiple samples prepared in a single deposition, as well as several measurements on the same sample.

A local maximum in electrical mobility and the best electrical conductivity were obtained for the least crystalline films. High mobility in amorphous materials can be attributed to the lack of grain boundaries. At small fractions of the crystalline material, if conduction is predominately through the amorphous phase, the presence of crystallites can decrease the mean-free path of electrons. This effect could explain the decrease in mobility for $T_G < 100\,^{\circ}\mathrm{C}$ in the semi-crystalline films. As the fraction of crystallinity increases, so does the grain size (inferred from Fig. 8). The increase in mobility for $T_G > 200\,^{\circ}\mathrm{C}$ could then be attributed to larger grains and less grain boundaries. Furthermore, as mentioned earlier, another interesting correlation between the mobility and peak shape exits. As shown in Fig. 3, for $75\,^{\circ}\mathrm{C} \leq T_G \leq 200\,^{\circ}\mathrm{C}$, along the out-of-plane direction, the diffraction peaks are asymmetric, and there is splitting of the (222) reflection, but at higher growth temperatures, the diffraction peaks become more symmetric and the splitting disappears. The splitting correlates well with low mobility of the crystalline films. The lowest μ is measured for $T_G = 100\,^{\circ}\mathrm{C}$, which corresponds to the largest splitting of the diffraction peaks and to a factor of 4 to 5 difference in deviatoric strain between these two lattices. The presence of two differently strained layers in the $T_G = 100\,^{\circ}\mathrm{C}$ sample is also consistent with a low electric mobility, as the mean-free path of electrons can be greatly decreased if they travel in such an anisotropic environment. The diffraction peaks for samples grown at higher temperatures are more symmetric while the mobility increases. The cross-over of the in-plane and out-of-plane lattice parameters at $T_G = 400\,^{\circ}\mathrm{C}$ represents zero deviatoric strain in the film as the interior of the film becomes more isotropic in the lateral direction. Furthermore, for this sample, the depth isotropy is also maximized since the in-plane lattice parameters for the interior and top of the film only vary by 0.002%, while the out-plane parameters differ by 0.029%. This combination of lateral and depth isotropy correlates with high electron mobility values. The work by Izumi *et al.* also reports similar trends in ITO: when the out-of-plane and in-plane parameters crossed over (corresponding to zero deviatoric strain), their lowest resistivity film was obtained.[20] For $T_G = 600\,^{\circ}\mathrm{C}$, the in-plane lattice parameters differ by 0.004%, while the out-of-plane variation is 0.090%. The deviatoric strain increases to 0.8% for $2\alpha_c$ and 1.5% for $1\alpha_c$. While this sample is slightly more anisotropic, the slight increase in mobility can be attributed to larger grain sizes where the number of scattering events with grain boundaries decreases.

The overall electrical conductivity obtained from Hall measurements for the films deposited above room temperature decreases as the deposition temperature increases. Since conductivity includes the effects of both the electron mobility and carrier concentration, the increase in mobility at higher deposition temperatures is overcome by the decrease in the carrier concentration. Figure 10 shows that the conductivity follows a decreasing trend similar to the behavior of the average of the in-plane and out-of-plane lattice parameters in the bulk of the film. As the deposition temperature is lowered, the average lattice parameter deviates more from the ideal IO value, resulting in a more conductive material, where a higher population of defects exist in a medium that allows them to be more mobile.

As mentioned in the Introduction, in-plane and cross-plane measurements of electrical[23,24] and thermal[24] conductivities on other materials show that electronic transport and thermal conductivity are highly anisotropic. The in-plane *vs* cross-plane electrical conductivity of Ge/Si films can vary by a factor of five, while the in-plane *vs* cross-plane thermal conductivities can differ significantly, by a factor of 675 in graphene oxide. Similar measurements on TCO materials have not been conducted, but as shown in the present study, the anisotropy of the structure and microstructure of PLD IO thin films varies widely, and one would expect that this anisotropy plays a major role in the properties of these and other transparent conducting oxides. A better understanding of these effects can help optimize the structure and microstructure of TCO films to enhance the desired properties for specific applications.

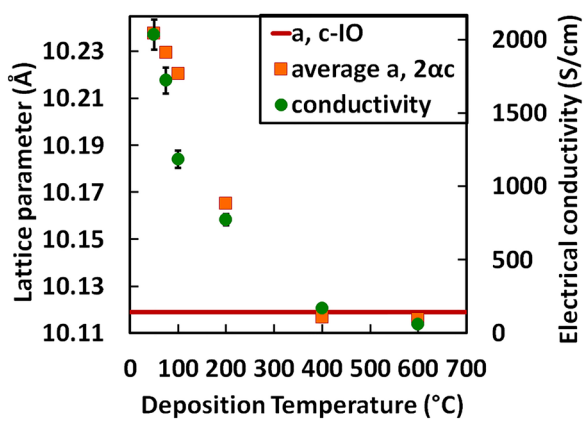

FIG. 10. Average lattice parameters and electrical conductivity as a function of deposition temperature for $2\alpha_c$. The uncertainties in the conductivity correspond to the standard deviation of measurements on multiple samples prepared in a single deposition, as well as several measurements on the same sample. The uncertainty in the lattice parameter was smaller than the symbol size.

IV. CONCLUSIONS

Indium oxide thin films grown via PLD at room temperature and above crystallized in the cubic bixbyite structure. The samples corresponding to early stages of crystallization showed a strong (400) preferred orientation which was more pronounced in the out-of-plane direction. As the deposition temperature increased, other IO bixbyite peaks appeared and the (400) preferred orientation decreased. The films exhibited both lateral anisotropy and depth anisotropy. Both at the surface and deeper in the films, higher distortions were observed in the out-of-plane than in the in-plane direction. Along the (222) and (332) reflections, the texture coefficient increased with deposition temperature and reached a maximum at 400 °C, while for the (440) reflection, it decreased. Higher texture coefficient differences were measured at the film surface compared to the interior of the film, indicating depth anisotropy. The lattice parameter increased in the in-plane direction but decreased in the out-of-plane direction as higher degrees of crystallinity were achieved. The deviatoric strain was linear both as a function of deposition temperature and the degree of crystallinity. The increased strain in films grown at higher temperatures could be attributed to differences in thermal expansion coefficients between the substrate and the films, while strain at lower temperatures can be due to the directional energy of the PLD species as they impinge on the substrate and to a double-layer structure that forms in semi-crystalline films. The low mobility values and asymmetric diffraction peaks along the out-of-plane direction were found to be correlated in semi-crystalline films. The minimum in the electrical mobility corresponded to the largest splitting of diffraction peaks for $T_G = 100\,^{\circ}\mathrm{C}$, which could be attributed to a double-layer structure with different deviatoric strain values, as well as to a film where small crystallites act as scattering centers for electrons. A weakly strained bottom layer could crystallize due to substrate annealing, while a highly strained layer with more disorder crystallizes at the top of the film. This depth and lateral anisotropy hinders the movement of electrons and correlates well with poor electron mobility. A further increase in deposition temperature resulted in samples that exhibited more symmetric diffraction peaks, less strain, higher crystallinity, and sharper peaks consistent with larger grain sizes where the electrons' mean-free path is expected to be longer, resulting in higher mobility. Higher temperatures of the substrate relax strain as the atoms can diffuse in all directions and become more ordered resulting in more isotropic films. The sample deposited at 400 °C exhibited the minimum deviatoric strain and the lowest depth anisotropy. This high lateral and depth isotropy correlated with high electron mobility, as the electrons can travel longer distances without being scattered by microstructural defects.

The lateral anisotropy and depth anisotropy results of the present study provide an increased understanding on the relationship between electrical properties and the changes in the structure and microstructure during the crystallization process. This knowledge not only can help improve the electrical performance of materials but also can be extended to optimizing thermal, mechanical, and optical properties of indium-based oxides, as well as other TCOs. A better understanding between the effects of the structure and microstructure on desirable properties is crucial in current applications and can open up future applications where mechanical flexibility, as well as high electrical and thermal conductivity, are desired.

ACKNOWLEDGMENTS

This project was funded by the NSF-MRSEC Grant No. DMR-1121262. The use of the Advanced Photon Source was supported by the Office of Science, Office of Basic Energy Sciences in the U.S. Department of Energy, under Contract No. DE-AC02-06CH11357. J. Boesso received funding from the Undergraduate Summer Research Program of the College of Science and Health at DePaul University.

[1]K. L. Chopra, S. Major, and D. K. Pandya, Thin Solid Films **102**, 1 (1983).
[2]D. S. Ginley and C. Bright, MRS Bull. **25**, 15–18 (2000).
[3]J. F. Wagner, D. A. Keszler, and R. E. Presley, *Transparent Electronics* (Springer, New York, 2008).
[4]E. Fortunato, D. Ginley, H. Hosono, and D. C. Paine, MRS Bull. **32**, 242–247 (2007).
[5]D. S. Ginley, H. Hosono, and D. C. Paine, *Handbook of Transparent Conductors* (Springer, New York, 2010).
[6]D. B. Buchholz, D. E. Proffit, M. D. Wisser, T. O. Mason, and R. P. H. Chang, Prog. Nat. Sci.: Mater. Int. **22**, 1–6 (2012).
[7]M. P. Taylor, D. W. Readey, M. F. A. M. van Hest, C. W. Teplin, J. L. Alleman, M. S. Dabney, L. M. Gedvilas, B. M. Keyes, B. To, J. D. Perkins, and D. S. Ginley, Adv. Funct. Mater. **18**, 3169–3178 (2008).
[8]W. M. Kim, D. Y. Ku, I.-K. Lee, Y. W. Seo, B.-K. Cheong, T. S. Lee, I.-H. Kim, and K. S. Lee, Thin Solid Films **473**, 315–320 (2005).
[9]M. Ito, M. Kon, C. Miyazaki, N. Ikeda, M. Ishizaki, R. Matsubara, Y. Ugajin, and N. Sekine, Phys. Status Solidi A **205**, 1885–1894 (2008).
[10]D. Y. Lee, J. R. Lee, G. H. Lee, and P. K. Song, Surf. Coat. Technol. **202**, 5718–5723 (2008).
[11]J. R. Bellingham, W. A. Phillips, and C. J. Adkins, J. Phys.: Condens. Matter **2**, 6207–6221 (1990).
[12]J.-H. Kim and J.-W. Park, Org. Electron. **14**, 3444–3452 (2013).
[13]B. Cui, L. Zeng, D. Keane, M. J. Bedzyk, D. B. Buchholz, R. P. H. Chang, X. Yu, J. Smith, T. J. Marks, Y. Xia, A. F. Facchetti, J. E. Medvedeva, and M. Grayson, J. Phys. Chem. C **120**, 7467–7475 (2016).
[14]M. Marezio, Acta Crystallogr. **20**, 723 (1966).
[15]G. B. González, T. O. Mason, J. P. Quintana, O. Warschkow, D. E. Ellis, J.-H. Hwang, J. P. Hodges, and J. D. Jorgensen, J. Appl. Phys. **96**, 3912 (2004).
[16]D. B. Buchholz, L. Zeng, M. J. Bedzyk, and R. P. H. Chang, Prog. Nat. Sci.: Mater. Int. **23**, 475–480 (2013).
[17]D. B. Buchholz, Q. Ma, D. Alducin, A. Ponce, M. José-Yacamán, R. Khanal, J. Medvedeva, and R. P. H. Chang, ACS Chem. Mater. **26**(18), 5401–5411 (2014).
[18]D. B. Buchholz, L. Zeng, M. J. Bedzyk, and R. P. H. Chang, Prog. Nat. Sci.: Mater. Int. **23**, 475–480 (2013).
[19]F. O. Adurodija, H. Izumi, T. Ishihara, H. Yoshioka, and M. Motoyama, J. Mater. Sci.: Mater. Electron. **12**, 57–61 (2001).
[20]H. Izumi, F. O. Adurodija, T. Kaneyoshi, T. Ishihara, H. Yoshioka, and M. Motoyama, J. Appl. Phys. **91**, 1213–1218 (2002).
[21]X. Z. Yan, X. Man, J. G. Ma, H. Y. Xu, and Y. C. Liu, J. Non-Cryst. Solids **423–424**, 18–24 (2015).
[22]C. H. Yi, Y. Shigesato, I. Yasui, and S. Takaki, Jpn. J. Appl. Phys., Part 2 **34**, L244–L247 (1995).
[23]V. Cracium, D. Cracium, X. Wang, T. J. Anderson, and R. K. Singh, Thin Solid Films **453–454**, 256–261 (2004).
[24]D. E. Proffit, Q. Ma, D. B. Buchholz, R. P. H. Chang, M. J. Bedzyk, and T. O. Mason, J. Am. Ceram. Soc. **95**(11), 3657–3664 (2012).
[25]D. E. Proffit, S. P. Harvey, A. Klein, R. Schafranek, J. D. Emery, D. B. Buchholz, R. P. H. Chang, M. J. Bedzyk, and T. O. Mason, Thin Solid Films **520**, 5633–5639 (2012).

[26]J. D. Renteria, S. Ramirez, H. Malekpour, B. Alonso, A. Centeno, A. Zurutuza, A. I. Cocemasov, D. L. Nika, and A. A. Balandin, Adv. Funct. Mater. **25**, 4664–4672 (2015).
[27]G. Fiedler, L. Nausner, Y. Hu, P. Chen, A. Rastelli, and P. Kratzer, Phys. Status Solidi A **213**, 524–532 (2016).
[28]J. Als-Nielsen and D. McMorrow, *Elements of Modern X-Ray Physics* (John Wiley & Sons, Ltd, 2011).
[29]A. P. Hammersley, S. O. Svensson, M. Hanfland, A. N. Fitch, and D. Hausermann, High Pressure Res. **14**, 235–248 (1996).
[30]See www1.aps.anl.gov/Sector-1/1-ID/Data-Analysis for MatWAXS.
[31]B. H. Toby and R. B. Von Dreele, J. Appl. Crystallogr. **46**, 544–549 (2013).
[32]P. Guo, R. D. Schaller, L. E. Ocola, J. B. Ketterson, and R. P. H. Chang, Nano Lett. **16**, 5639–5646 (2016).
[33]W.-F. Wu and B.-S. Chiou, Thin Solid Films **298**, 221–227 (1997).
[34]D. Bhattacharyya and M. J. Carter, Thin Solid Films **288**, 176–181 (1996).
[35]See https://accuratus.com/fused.html for fused silica properties.
[36]M. Quaas, H. Steffen, R. Hippler, and H. Wulff, Surf. Sci. **540**, 337–342 (2003).